Science Bulletin 64 (2019) 1502–1509

Contents lists available at ScienceDirect

Science Bulletin

journal homepage: www.elsevier.com/locate/scib

Science Bulletin
www.scibull.com

Article

Improving the photocatalytic hydrogen evolution of UiO-67 by incorporating Ce^{4+}-coordinated bipyridinedicarboxylate ligands

Yang An [a,b], Yuanyuan Liu [a,*], Hongtao Bian [c], Zeyan Wang [a], Peng Wang [a], Zhaoke Zheng [a], Ying Dai [d], Myung-Hwan Whangbo [a,e,f], Baibiao Huang [a,*]

[a] State Key Laboratory of Crystal Materials, Shandong University, Jinan 250100, China
[b] Institute for Innovative Materials and Energy, Yangzhou University, Yangzhou 225002, China
[c] Key Laboratory of Applied Surface and Colloid Chemistry, Shaanxi Normal University, Xi'an 710119, China
[d] School of Physics, Shandong University, Jinan 250100, China
[e] Department of Chemistry, North Carolina State University, Raleigh, NC 27695-8204, USA
[f] State Key Laboratory of Structural Chemistry, Fujian Institute of Research on the Structure of Matter (FJIRSM), Chinese Academy of Sciences, Fuzhou 350002, China

ARTICLE INFO

Article history:
Received 5 May 2019
Received in revised form 1 July 2019
Accepted 23 July 2019
Available online 29 July 2019

Keywords:
MOFs
UiO-67
Bipyridine-tetravalent cerium
Photocatalytic hydrogen evolution
Energy transfer

ABSTRACT

UiO-67 is a Zr-based metal–organic framework (MOF) containing an organic linker namely, the dianion of biphenyl-4,4′-dicarboxylic acid (bpdc). Ce^{4+} metal ions (0.02 Ce to Zr atom ratio) were incorporated into UiO-67 via partially replacing bpdc with the dianion of 2,2′-bipyridine-5,5′-dicarboxylic acid (bpydc); thus, the latter forms a bpydc-Ce complex. The resulting product (i.e., UiO-67-Ce) demonstrated a photocatalytic hydrogen evolution rate that was over 10 times higher than that of UiO-67. Through this modification, a new energy transfer channel is opened up. The energy transfer between the bpdc and bpydc-Ce ligands (i.e., from excited bpdc to bpydc-Ce) weakened the recombination of the charge carriers, which was confirmed by photoluminescence, emission lifetime, and transient absorption measurements. This study presents a new way to construct highly efficient MOF photocatalysts.

1. Introduction

Nowadays, the problem of energy shortage is becoming critical. Photocatalytic water splitting can provide a green way to produce H_2 and relieve the energy shortage crisis [1–9]. Metal–organic frameworks (MOFs) produced using organic linkers (i.e., multidentate ligands) and metal-based nodes, are attracting tremendous interests as promising alternative photocatalysts [10–19]. It has been believed that the photocatalytic activities of MOFs arise from the ligand to metal charge transfer (LMCT) process [20], but our previous study [21] demonstrated that ligand-to-ligand charge transfer (LLCT) process can provide a new pathway of the electron transfer leading to a higher photocatalytic activity.

The structural and functional tunability of MOFs enables preparing MOFs comprising more than one linker. Such MOFs have been reported to display improved photocatalytic activities. The MOF, UiO-66, is based on the organic linker benzene dicarboxylates (bdc). Maligal-Ganesh and co-workers [22] prepared samples of UiO-66 by replacing some bdc either with bdc-NH_2 (i.e., bdc with electron-donating substituent NH_2) or bdc-X (i.e., bdc with electron-withdrawing group X = F, Cl or Br) and determined an improved photocatalytic activity for alcohol oxidation. Another MOF, Ti-based MIL-125, is also based on bdc. Mellot-Draznieks and co-workers [23] prepared samples of MIL-125 based on both bdc and bdc-NH_2 and determined that the highest photocatalytic activity for benzyl alcohol oxidation was obtained with the bdc-NH_2 to bdc ratio of 50%.

The MOF, UiO-67, is based on the organic linker bpdc (i.e., the dianion of biphenyl-4,4′-dicarboxylic acid). The organic linker bpydc (i.e., the dianion of 2,2′-bipyridine-5,5′-dicarboxylic acid) is often used as a ligand to anchor various catalytic active metals/metal complexes in MOFs [24]. In several studies, bpydc was incorporated into UiO-67 to attach complexes of Re, Ru, Rh, Pt or Pd to UiO-67 [25–28]. The resulting UiO-67 materials were found to display efficient photocatalytic CO_2 reduction, water oxidation or other catalytic activities [29,30]. In a similar manner, complexes of Cu, Co or Mn can be incorporated into UiO-67 [31–33]. In general, the transition metal complexes incorporated into MOFs act as active sites for photocatalytic activities via the LMCT process.

So far as we know, only a few studies have examined the interaction between different linkers in MOFs and energy transfer between them leading to photocatalytic activities [25,32,34–36]. It is known that Ce can promote energy transfer due to its

* Corresponding authors.
E-mail addresses: yyliu@sdu.edu.cn (Y. Liu), bbhuang@sdu.edu.cn (B. Huang).

https://doi.org/10.1016/j.scib.2019.07.030
2095-9273/

low-lying empty 4f orbitals and act as active sites for H_2 evolution [37–42]. In this work, we introduced Ce^{4+} into UiO-67 to form UiO-67-Ce by replacing some bpdc of UiO-67 with bpydc-Ce (namely, a complex formed by bpydc coordinated with Ce^{4+}) and demonstrated that the photocatalytic H_2 evolution rate is greatly enhanced over UiO-67-Ce than UiO-67. Our analysis suggests that the introduction of Ce weakens the LMCT process and opens up a new energy transfer channel from bpdc to bpydc-Ce. Additionally, the introduction of Ce not only promotes the energy transfer but also acts as active sites for H_2 evolution.

2. Experimental

2.1. Materials

All of the reagents were of analytical grade and were used without any purification. $ZrCl_4$ (98%) was ordered from Acros Organics, C_6H_5COOH (>99.5%), HCl (36 wt%–38 wt%), biphenyl-4,4′-dicarboxylic acid (H_2bpdc) was purchased from Aladdin Industrial Corporation, methyl alcohol from Sinopharm Chemical Reagent Co., ceric ammonium nitrate from Kermel, 2,2′-bipyridine-5,5′-dicarboxylic acid (H_2bpydc) from TCI, ethanol and *N*,*N*-dimethylformamide (DMF) were purchased from Tianjin Fuyu Fine Chemical Co.

2.2. Synthesis of UiO-67 and UiO-67-Ce

2.2.1. UiO-67

$ZrCl_4$ (0.120 g, 0.514 mmol), C_6H_5COOH (1.256 g, 10.29 mmol, for pore-making) and HCl (0.36 g, 10 mmol, to inhibit the hydrolysis of absolute $ZrCl_4$) were mixed in 20 mL DMF. Then H_2bpdc (0.114 g, 0.469 mmol) was added to the above clear solution. After stirring for 10 min at room temperature, the precursor solution was introduced into a 100 mL Teflon-lined autoclave and kept at 120 °C for 24 h. After cooling to room temperature naturally, a white solid was obtained. The solid was washed with DMF and suspended in DMF at room temperature for 12 h. Then the solid was recovered by filtration and suspended in methyl alcohol (CH_3OH) at room temperature for another 12 h. Finally, the obtained solid was washed with ethanol and dried under reduced pressure for further use.

2.2.2. UiO-67-Ce

Ceric ammonium nitrate (0.274 g, 0.5 mmol) and H_2bpydc (0.122 g, 0.5 mmol) were mixed in 120 mL CH_3OH. After stirring for 2 d at room temperature, the solid of H_2bpydc-Ce was obtained.

$ZrCl_4$ (0.120 g, 0.514 mmol), C_6H_5COOH (1.256 g, 10.29 mmol) and HCl (0.36 g, 10 mmol) were mixed in 20 mL DMF. After stirring to the clear solution, H_2bpdc (0.113 g, 0.465 mmol) and H_2bpydc-Ce (25 mg, 0.05 mmol) were added (Scheme 1). Then after stirring for 10 min at room temperature, the precursor solution was introduced into a 100 mL Teflon-lined autoclave and kept at 120 °C for 24 h. After cooling to room temperature naturally, a white solid was obtained. The solid was washed with DMF and suspended in DMF at room temperature for 12 h. Then the solid was recovered by filtration and suspended in methyl alcohol at room temperature for another 12 h. The obtained particles were washed with ethanol and dried under reduced pressure for further use.

2.3. Characterizations

The X-ray powder diffraction (XRD) measurement of the as-prepared sample was performed on an X-ray powder diffraction (Bruker AXS D8). Elementary composition of UiO-67 and UiO-67-Ce was performed on Elementar (Vario EL CUBE). A Micromeritics ASAP 2020 analyzer was applied to measure the Brunauer-Emmett-Teller (BET) surface areas of the samples at liquid nitrogen temperature. Before the measurement of BET surface area, the as-prepared samples were pretreated at 150 °C under vacuum for 8 h. The morphology of the samples and energy dispersive X-ray spectrum (EDS) were characterized by scanning electron microscopy (SEM, Hitachi S-4800). The inductively coupled plasma-mass spectroscopy (ICP-MS) was determined by Optima 2100DV: UiO-67-Ce powders before and after hydrogen evolution reaction (HER) were acid digested into transparent solution. The concentration of Zr and Ce were determined to be 395.444/227.083 and 12.049/6.865 mg/L, respectively. X-ray photoelectron spectroscopy (XPS) analysis was characterized on a Thermo Fisher Scientific Escalab 250 spectrometer and C 1s (284.6 eV) was used to calibrate the peak positions. Fourier transform infrared (FT-IR) spectra were obtained using a Bruker ALPHA-T spectrometer with KBr pellets. The UV–Vis diffuse reflectance spectra (DRS) was performed on a Shimadzu UV 2550 recording spectrophotometer, which was equipped with an integrating sphere and $BaSO_4$ was used as a reference. Photoluminescence (PL) spectra were obtained on an F-4500 FL Spectrophotometer. The size measurement was carried out using the dynamic light scattering (DLS) method with a Malvern instrument. Electron paramagnetic resonance (EPR) measurements were performed on a Bruker A300 spectrometer with a microwave power of 8 mW, a modulation frequency of 100 kHz and modulation amplitude of up to 5 G, in aqueous CH_3OH solutions 77 K. Steady state and time resolved fluorescence spectra were carried out on an Edinburgh FLS980 high sensitivity fluorescence spectrometer.

The setup for femtosecond transient absorption (TA) is based on a regenerative amplified Ti: sapphire laser system from HARPIA (800 nm, 1 kHz repetition rate), nonlinear frequency mixing techniques and the transient absorption spectrometer (Keramiku 2B,

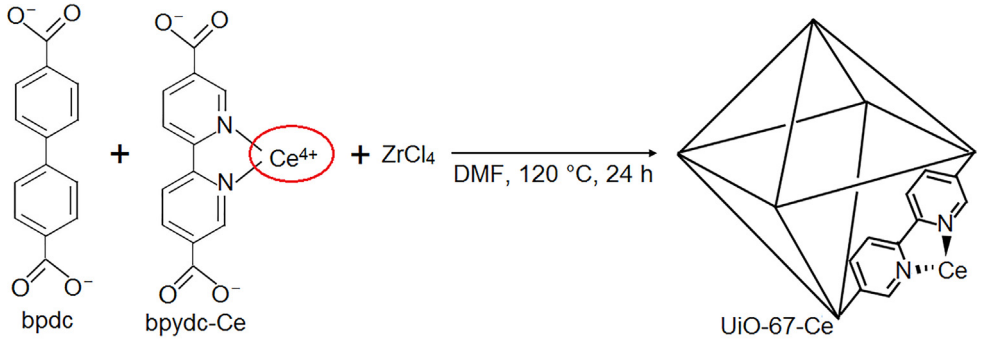

Scheme 1. (Color online) Preparation process of UiO-67-Ce.

LT-10233). The 800 nm output pulse from the regenerative amplifier was split into two parts. The transmitted part was used to pump an Optical Parametric Amplifier (OPA). The reflected 800 nm beam was split again into two parts. One part was attenuated with a neutral density filter and focused into a 2 mm thick sapphire window to generate a white light continuum (WLC) from 420 to 800 nm used as the probe beam.

2.4. Photocatalytic reaction

Photocatalytic HER was carried out in a top-irradiation vessel connected to a glass-enclosed gas circulation system. In a typical procedure, 25 mg of catalyst was suspended in 50 mL aqueous solution (water/CH_3OH = 4/1, volume ratio) with constant stirring. The pH value used for photocatalytic HER was ~4.85. Before photocatalytic reactions, the suspension was exposed to ultrasonic treatment for 10 min. The reaction temperature was maintained at 15 °C. Light source, Xe lamp (300 W, 18 A). The amount of H_2 evolved was determined by using a gas chromatograph (Shiweipx GC-7806), Ar as carrier gas.

3. Results and discussion

3.1. Characterization

The XRD patterns of the as-synthesized UiO-67 and UiO-67-Ce, presented in Fig. 1a, are in good agreement with the simulated UiO-67 and those reported previously [28,30,43,44]. UiO-67-Ce displays almost similar peaks to UiO-67, indicating that UiO-67-Ce and UiO-67 have the same framework structure. The three sharp peaks at 5.62° (1 1 1), 6.46° (0 0 2) and 9.18° (0 2 2) for the synthesized samples indicated that they were highly crystalline. Besides, the peaks at 11.33°, 13.06°, 23.59°, 30.26° and 37.06° are the diffraction of (1 1 3), (0 0 4), (1 1 5), (2 2 4) and (1 3 7) crystal planes of UiO-67. The analysis of N_2 adsorption-desorption isotherms at 77 K (Fig. 1b) shows a smaller BET surface area for UiO-67-Ce (1,545 m^2/g) than for UiO-67 (1,638 m^2/g), which is due to the incorporation of Ce [28]. The SEM images of UiO-67 and UiO-67-Ce display the same morphology (Fig. 1c, d), namely, cubic particles with the size of ~100 nm. This demonstrates that the incorporation of Ce causes almost no change in the particle size and morphology of UiO-67.

Besides, the atom compositions (in atomic %) of UiO-67 and UiO-67-Ce were determined by both EDS and elemental analyses. The results are as follows (the numbers in the parentheses are theoretical values). For UiO-67, Zr: 3.36 (3.45), C: 48.24 (48.28), H: 30.08 (29.88), O: 18.32 (18.39). For UiO-67-Ce, Zr: 3.32, C: 48.29, H: 29.89, O: 18.30, N: 0.132, Ce: 0.066. Therefore, the chemical formulas for the UiO-67 and UiO-67-Ce samples are $Zr_6O_4(OH)_4(bpdc)_6$ and $Zr_6O_4(OH)_4(bpdc)_{5.88}(bpydc\text{-}Ce)_{0.12}$, respectively. So, the replacement ratio of bpydc is 2%.

The presence of Ce in UiO-67-Ce was confirmed by XPS measurement (Fig. 2). The Ce 3d peak at 877.8 eV can be assigned to Ce^{4+} [45–47]. The observed Ce 3d peak was really weak, showing very few loading amounts of Ce ions. The N 1s XPS peaks of UiO-67-Ce at 398.8 and 401.9 eV are assigned to the N–C and N–Ce bonds of bpydc-Ce [48,49], respectively (Fig. S1a, b online). Besides, the Zr 3d peaks are at the same position for both UiO-67 and UiO-67-Ce (Fig. S1c online). These results suggest that Ce^{4+} ions are coordinated to the N of the pyridine ring linker rather than to the carboxylate oxygen or just adsorbed on UiO-67. The EDS analysis suggests that the Zr to Ce atom ratio is 1:0.02 (Fig. S2 online), showing a small amount of bpydc-Ce was incorporated. However, the Ce content in UiO-67-Ce does not increase if further increasing

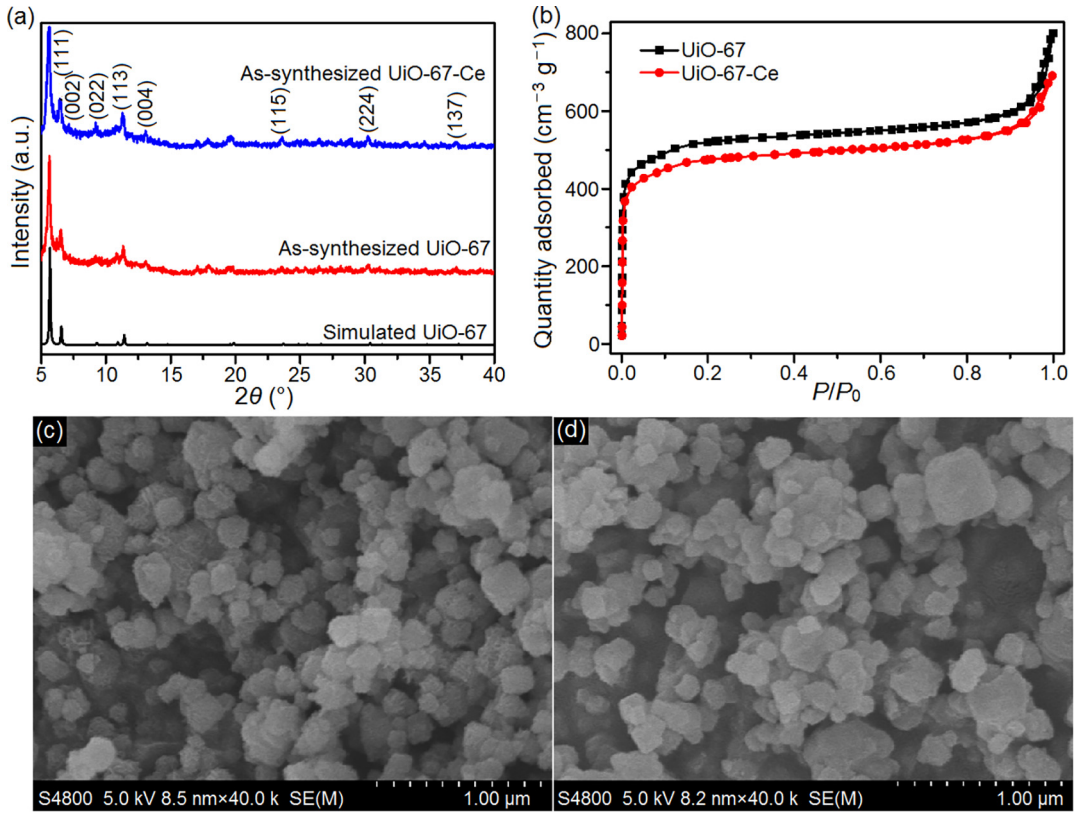

Fig. 1. (Color online) Structure and morphology of UiO-67 and UiO-67-Ce. (a) XRD patterns of the simulated UiO-67, the as-synthesized UiO-67 and the as-synthesized UiO-67-Ce. (b) N_2 adsorption-desorption isotherms of the as-prepared UiO-67 and UiO-67-Ce. SEM images of (c) UiO-67 and (d) UiO-67-Ce.

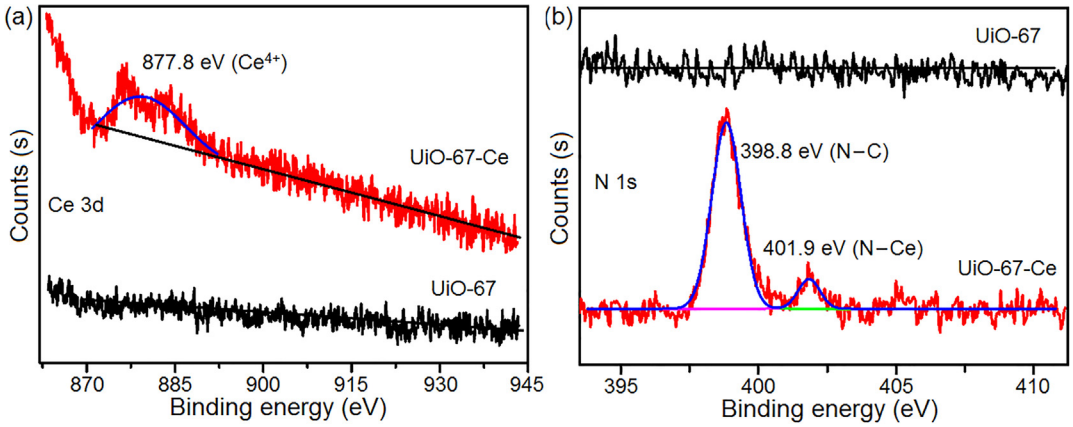

Fig. 2. (Color online) XPS spectra for (a) Ce 3d and (b) N 1s of UiO-67 and UiO-67-Ce.

the content of bpydc-Ce during the synthesis process of UiO-67-Ce. The reason is most likely that more bpydc-Ce would destroy the framework structure of UiO-67. The content of Ce and Zr in UiO-67-Ce were also measured by ICP-MS. The Ce/Zr atom ratio was 0.018, which was consistent with the EDS data.

The FT-IR spectra of UiO-67 and UiO-67-Ce are shown in Fig. 3. Upon introducing bpydc-Ce, the majority of peaks remain the same while minor differences can be observed between the spectra of UiO-67-Ce and UiO-67. One peak of UiO-67 at 1,418 cm^{-1} (the C–C stretching vibrations of the benzene ring and pyridine ring) moves to 1,413 cm^{-1} in UiO-67-Ce. The reason is that Ce–N bond formation would weaken the C–C bond in bpydc as a consequence of electron transfer from N to Ce, suggesting the presence of bpydc-Ce in UiO-67-Ce. Furthermore, the single peak of UiO-67 at 1,700 cm^{-1} splits into two peaks in UiO-67-Ce. This is attributed to the presence of the C=N bonds in the pyridine ring in bpydc-Ce [50–52].

3.2. Photocatalytic performance

The photocatalytic activities over UiO-67 and UiO-67-Ce were checked in terms of HER from water (Fig. 4). UiO-67-Ce exhibits much higher HER rate than UiO-67 does. The HER rate over UiO-67-Ce is 269.6 μmol/(g h), more than 10 times higher than that over UiO-67 (26.78 μmol/(g h) under the same experiment conditions). Both of them have no photocatalytic hydrogen production

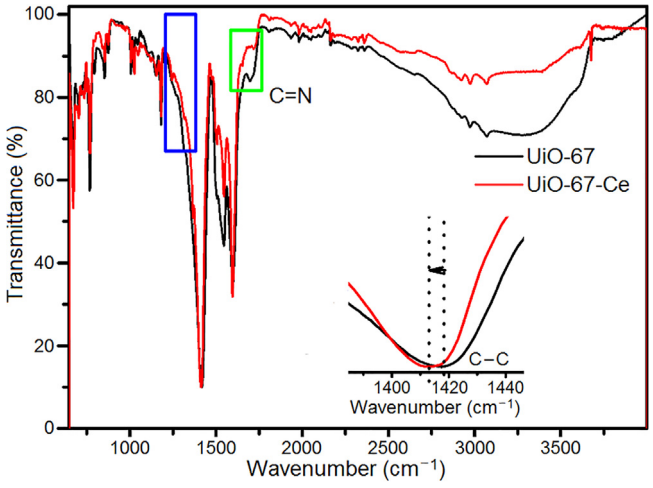

Fig. 3. (Color online) FT-IR spectra of UiO-67 and UiO-67-Ce, and the inset shows an enlarged image.

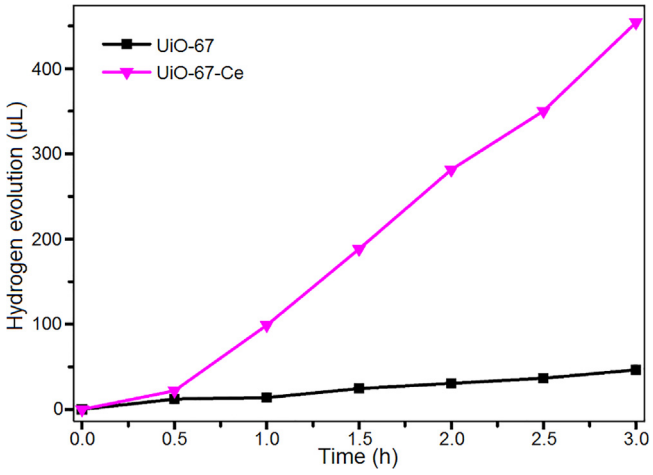

Fig. 4. (Color online) Photocatalytic hydrogen evolution over UiO-67 and UiO-67-Ce. Reaction conditions: 25 mg of catalysts, 50 mL methanol (electron donor) aqueous solutions (pH 4.85). Light source, Xe lamp (300 W).

activity under visible light ($\lambda > 400$ nm). In addition, UiO-67-Ce MOF outperforms the previously reported Zr-based MOF photocatalysts in the photocatalytic hydrogen evolution reaction [51,53,54]. All of the above confirms that the introduction of bpydc-Ce into UiO-67 can greatly improve the photocatalytic hydrogen evolution from water. The Ce/Zr atom ratio was also determined after the photocatalytic reaction by ICP-MS, and the value is 0.019, which is consistent with the value before the photocatalytic reaction. In addition, no Ce ions can be detected in the supernatant after photocatalytic reaction. This result suggests that UiO-67-Ce is stable during the photocatalytic process.

Furthermore, the H_2 evolution rate over UiO-67-Ce under UV/Vis irradiation decreased after 6 h. This suggests a decrease in the relative stability (Fig. S3a online). And the incorporation of Ce^{4+} does not affect the stability of UiO-67 (Fig. S3b online). The structure and physical properties of the UiO-67-Ce particles were checked after 12 h of photocatalytic H_2 evolution to uncover the reason for the activity decrease. As shown in Fig. S4a (online), the intensity of the XRD peaks decrease suggesting the decrease of crystallinity, which is the most likely induced by the collapse of the framework structure during the longtime photocatalytic reaction. The SEM images (Fig. S4b, c online) suggest that the morphologies of UiO-67-Ce change after photocatalytic reaction, namely, the cubic particles with a size of ~100 nm become irregular larger particles with a size range of 100–600 nm. These results

show that the framework structure of UiO-67-Ce was collapsed and destroyed during the photocatalytic process, which is the main reason for the observation that the H_2 evolution decreases after 6 h. We speculate that the framework structure of UiO-67-Ce was collapsed and destroyed due to the attack of the strong HO^- nucleophile in water and the continuous mechanical stirring during the longtime photocatalytic reaction [11].

The photocatalytic activities over bpydc and bpydc-Ce were checked to verify the effect of Ce on the HER (Fig. S5 online). The analysis demonstrated that bpydc leads to no H_2 production, but bpydc-Ce to an increasing amount of H_2 production over time. It suggests that Ce^{4+} acts as the active site for the hydrogen evolution [41,42]. Nevertheless, the HER rate over bpydc-Ce is 2.95 μmol/(g h) far less than that over UiO-67-Ce. This demonstrates the superiority of MOFs in photocatalytic activity, which prevents the chromophores from aggregation and consequently suppresses the self-quenching and deleterious attenuation of exciton lifetimes [55]. In addition, the photocatalytic activity for the sample without Ce, UiO-67-Y (the same ligand ratio of bpdc to bpydc as UiO-67-Ce but without Ce), was also investigated. As presented in Fig. S6 (online), UiO-67-Y shows a slight increase in the activity compared with UiO-67, but still much worse than that of UiO-67-Ce. This result indicates that the Ce incorporation plays a more important role in improving the photocatalytic activity than the bpydc ligand. Besides that, the photocatalytic activity of UiO-67 was also investigated with the presence of equal amount of Ce to UiO-67-Ce, (1) directly mixing UiO-67 and ceric ammonium nitrate in methanol for 24 h at R.T. and (2) heating the UiO-67 and ceric ammonium nitrate mixture at 120 °C for 24 h in DMF before isolation. For either case, the sample displays lower activity than UiO-67, implying the essential role of bpydc in helping Ce ions incorporated into UiO-67 for improving the photocatalytic activity (Fig. S7 online). The SEM and DLS results show that the as-prepared UiO-67 and UiO-67-Ce samples display almost the same size (100 nm) and aggregation (450 nm) in aqueous solutions (Fig. S8 and Table S1 online). Thus, the impact of the aggregation on the catalytic activity can be excluded.

3.3. Exploration of possible mechanism

We further explored the effect of bpydc-Ce on the photophysical properties. Fig. 5a compares the UV/Vis light absorption of UiO-67 and UiO-67-Ce. UiO-67-Ce displays a slight blue shift in the absorption edge (365 nm) and a greatly increased absorption intensity in the UV region, compared with UiO-67, due to the coordination of bpydc-Ce with Zr. Band gaps of UiO-67 before and after Ce loading are 3.02 and 3.39 eV. The DRS spectra in Fig. S9a (online) suggests that the ligand bpydc-Ce displays a much stronger intensity in the UV region than bpdc does, which is due to the larger absorption coefficient of bipyridine [56]. But if Ce as metal nodes of MOFs connected with the carboxylate oxygen in bpydc, such as MOF Ce-UiO-66-bpydc (a MOF constructed with Ce metal nodes and bpydc organic ligands) [57], the absorption edge will have a large red shift than bpydc (Fig. S10 online). This can also be the evidence that Ce coordinates to the N atoms in bpydc linkers rather than replace the positions of zirconium atoms connected with carboxylate in UiO-67. The excited state properties of UiO-67 and UiO-67-Ce were also investigated by PL spectra (Fig. 5b). Two emission peaks at 398 and 467 nm are observed for UiO-67-Ce, which are similar to that of bpydc-Ce (Fig. S9b online), implying that the emission of bpydc-Ce dominates over the radiative decay, although the concentration of bpydc-Ce is very low and the emission of bpdc observed in UiO-67 is almost quenched for UiO-67-Ce. In addition, UiO-67-Ce displays a much weaker peak than does UiO-67, suggesting that the photogenerated electron-hole pairs separate more efficiently in UiO-67-Ce than that in UiO-67, which agrees well with the observation that the H_2 evolution rate is much higher over UiO-67-Ce than that over UiO-67.

To further verify the electron transfer channel in UiO-67-Ce, the EPR spectra were carried out (Fig. 6a). An EPR signal is detected for both UiO-67-Ce and UiO-67 with the g-value of about 2.002, which is attributed to the formation of Zr^{3+} due to the reported LMCT process [54]. However, the Zr^{3+} signal is much weaker in UiO-67-Ce than UiO-67 under the same experiment conditions. Besides, no Zr^{3+} EPR signal was detected in the dark over UiO-67 and UiO-67-Ce (Fig. S11 online). This phenomenon suggests that the LMCT process happened with the presence of UV/Vis illumination is weakened in UiO-67-Ce due to the presence of bpydc-Ce. We assume that the presence of bpydc-Ce in UiO-67-Ce opens up a new energy transfer channel, i.e., from excited bpdc to bpydc-Ce, which is a competing process to the LMCT.

Considering the fact that the emission spectrum of bpdc displays a good overlap with the absorption spectrum of bpydc-Ce (Fig. S12 online) and the distance between bpdc and bpydc is less than ~ 7.88 Å, it is most likely that the Förster energy transfer occurs from the excited bpdc to bpydc-Ce [29,36,50,58,59]. To prove this possibility, we prepared mixtures of UiO-67 with bpdc, bpydc or bpydc-Ce, and studied their emission (excited at 300 nm) for fluorescence quenching effect. The concentration of bpdc, bpydc and bpydc-Ce are the same, that is, 0.2 mmol/L. Fig. 6b shows that the emission intensity of UiO-67 + bpdc is a slightly higher than UiO-67, while that of UiO-67 is greatly suppressed

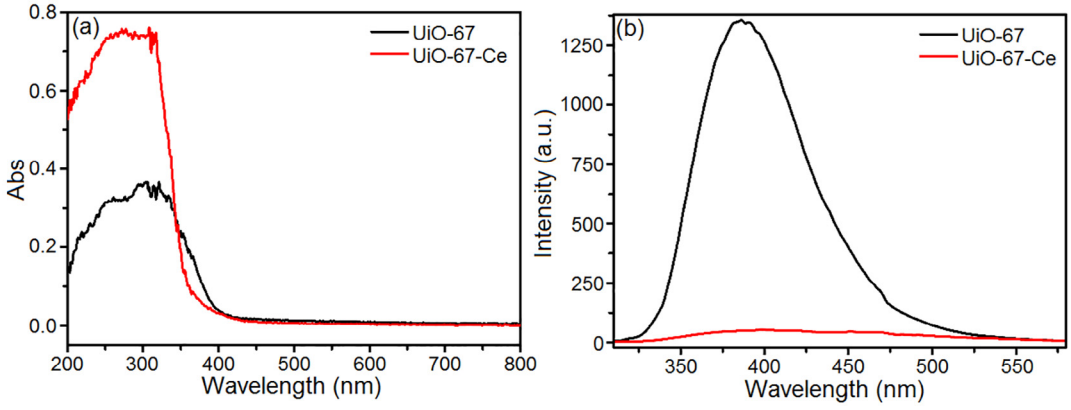

Fig. 5. (Color online) Photophysical properties of UiO-67 and UiO-67-Ce. (a) UV/Vis DRS and (b) PL spectra of UiO-67 and UiO-67-Ce, excited at 300 nm.

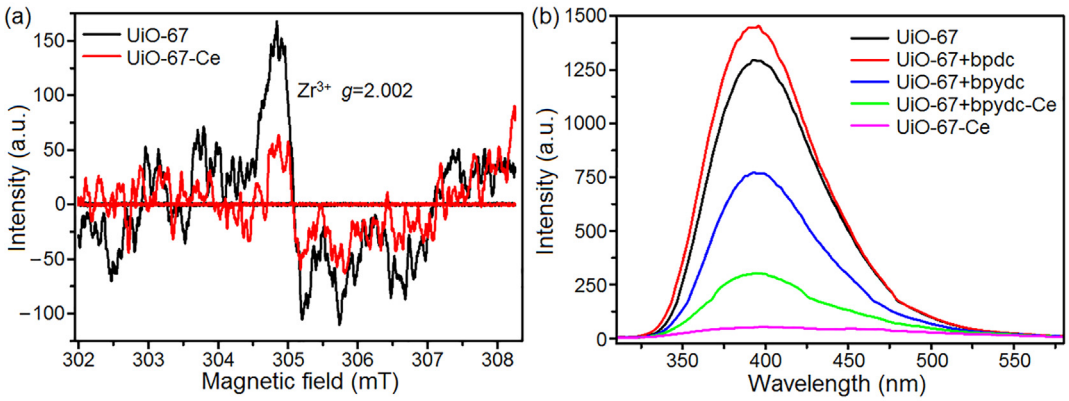

Fig. 6. (Color online) Photophysical excitation performance of UiO-67 and UiO-67-Ce. (a) EPR spectra of UiO-67 and UiO-67-Ce with the presence of UV/Vis illumination. (b) The PL spectra of UiO-67, UiO-67 + bpdc, UiO-67 + bpydc, UiO-67 + bpydc-Ce and UiO-67-Ce, excited at 300 nm, and "+" stands for physical mixing.

with the presence of bpydc and even more for bpydc-Ce. The PL and EPR results indicate that energy transfer occurs between bpdc and bpydc-Ce in UiO-67-Ce.

The energy transfer process occurred in UiO-67-Ce MOF is confirmed by time-resolved PL spectra (Fig. 7). The decay of the excited state of UiO-67-Ce is much faster than that of UiO-67, while the average lifetime is 6.56 and 2.92 ns for UiO-67 and UiO-67-Ce, respectively. The reduction of the fluorescence lifetime of UiO-67 in the presence of bpydc-Ce means the occurrence of energy transfer from bpdc to bpydc-Ce, in addition to the fluorescence back to the ground state of bpdc. This result indicates an evident energy transfer between bpdc and bpydc-Ce.

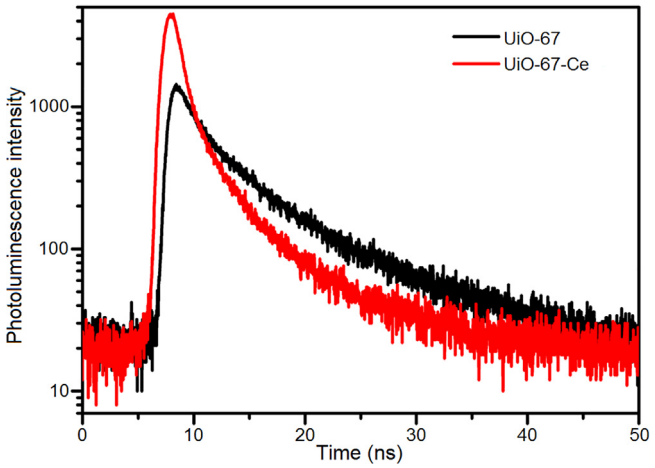

Fig. 7. (Color online) Time-resolved PL spectra for UiO-67 and UiO-67-Ce detected at 385 and 398 nm, respectively. The excitation source is a 340 nm laser.

The TA spectra of UiO-67 and UiO-67-Ce MOFs at different delay times after 300 nm excitation are compared in Fig. 8. The TA spectra of UiO-67 exhibits negative ground state bleach (GSB) signal at ~425 nm, which overlaps with a broad positive excited state absorption (ESA) signal from 505 to 750 nm. In contrast, the initiative ESA amplitude is blue-shifted in UiO-67-Ce, leaving a somewhat long-lived GSB signal compared to that of UiO-67. The GSB of UiO-67-Ce is blue-shifted (by ~56 nm) compared to that of UiO-67 (at ~369 nm), which is consistent with the result of DRS. There is a small sharp peak at 579 nm in both UiO-67 and UiO-67-Ce, which is assigned to the intrinsic ESA of Zr-moiety in MOFs. For UiO-67, after a sufficiently long delay time, the transient signal at 579 nm becomes strongly negative, indicating the occurrence of the electron transfer from ligands bpdc to the Zr metal nodes of UiO-67 during the TA spectra study. However, the corresponding peak in UiO-67-Ce becomes weak and remains positive after a sufficiently long delay time, which is consistent with the result of EPR, and the ESA decay and GSB recovery occur simultaneously [60–63]. This spectroscopic feature further confirms the existence of the energy transfer between bpdc and bpydc-Ce, inhibiting the electron transfer from bpdc to Zr in UiO-67-Ce.

Based on the above discussions, a photocatalytic mechanism for the enhanced photocatalytic H_2 evolution of UiO-67-Ce can be proposed as illustrated in Scheme 2. For UiO-67, the UV/Vis illumination induces the electron transfer from the excited bpdc to the

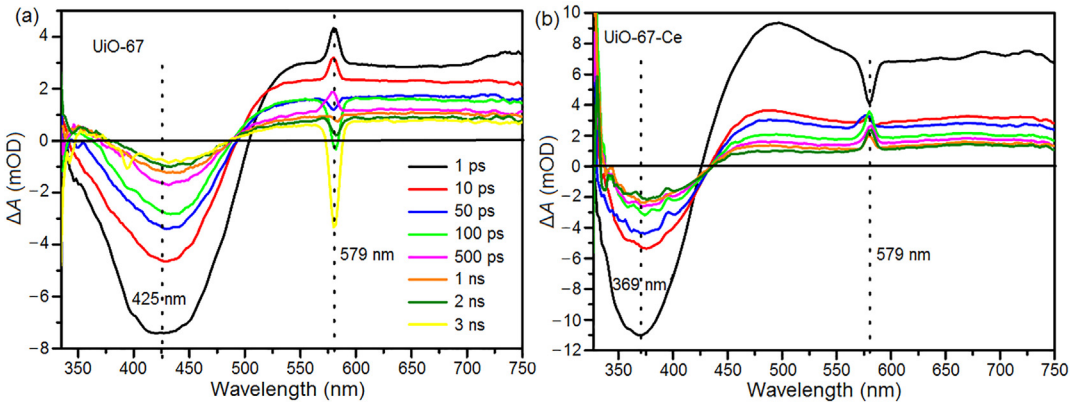

Fig. 8. (Color online) TA spectra of (a) UiO-67 and (b) UiO-67-Ce at various time delays, respectively.

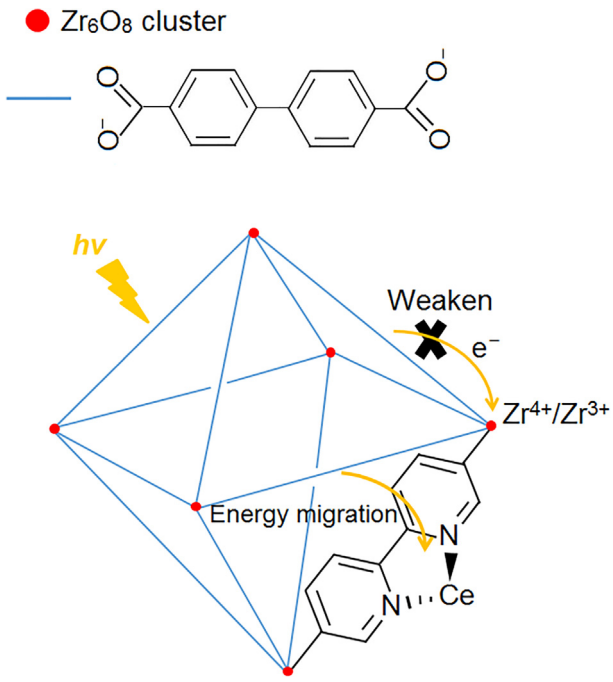

Scheme 2. (Color online) Proposed photocatalytic mechanism of photocatalytic hydrogen production reaction over UiO-67-Ce for easy demonstration.

zirconium-oxo cluster (LMCT process), resulting in the formation of Zr^{3+}. For UiO-67-Ce, the introduction of bpydc-Ce weakens the LMCT process and promotes the energy transfer from excited bpdc to bpydc-Ce.

4. Conclusions

In summary, Ce^{4+} was incorporated into UiO-67 containing bpydc as a mixed linker, based on the previous research [24,28,31–33]. The obtained UiO-67-Ce displays a much higher photocatalytic HER efficiency than UiO-67. The time-resolved and steady-state fluorescence spectra, transient absorption spectra and electron paramagnetic resonance spectra suggest that the presence of bpydc-Ce provides an alternative energy transfer channel [42,58,59] between bpdc and bpydc-Ce. This new energy transfer channel not only suppresses the recombination of photogenerated electrons and holes but also weakens the well-accepted LMCT process in UiO-67 [20,54], both of which are responsible for the improved photocatalytic activity of UiO-67-Ce. This work provides an alternative approach to improve the photocatalytic activities of MOFs, in addition to a deep understanding of the interaction between different linkers in MOFs comprising more than one linker.

Conflict of interest

The authors declare that they have no conflict of interest.

Acknowledgments

This work was supported by the National Natural Science Foundation of China (21333006, 21573135, U1832145, 11374190, 51321091, and 51602179), Taishan Scholar Foundation of Shandong Province, China, and Young Scholars Program (2016WLJH16).

Author contributions

Yang An prepared all the samples and carried out the experiments; Hongtao Bian assisted the TA test; Baibiao Huang, Zeyan Wang, Peng Wang, Zhaoke Zheng and Ying Dai co-supervised the project; Yang An, Yuanyuan Liu and Myung-Hwan Whangbo co-wrote the paper; Yang An, Yuanyuan Liu, Baibiao Huang and Myung-Hwan Whangbo discussed the results and commented on the manuscript.

Appendix A. Supplementary material

Supplementary material to this article can be found online at https://doi.org/10.1016/j.scib.2019.07.030.

References

[1] Li S, Wang Y, Peng S, et al. Co-Ni-based nanotubes/nanosheets as efficient water splitting electrocatalysts. Adv Energy Mater 2016;6:1501661.
[2] Wu Y, Wang P, Zhu X, et al. Composite of $CH_3NH_3PbI_3$ with reduced graphene oxide as a highly efficient and stable visible-light photocatalyst for hydrogen evolution in aqueous HI solution. Adv Mater 2018;30:1704342.
[3] Wang X, Maeda K, Thomas A, et al. A metal-free polymeric photocatalyst for hydrogen production from water under visible light. Nat Mater 2009;8:76–80.
[4] Wu Y, Wang P, Guan Z, et al. Enhancing the photocatalytic hydrogen evolution activity of mixed-halide perovskite $CH_3NH_3PbBr_{3-x}I_x$ achieved by bandgap funneling of charge carriers. ACS Catal 2018;8:10349–57.
[5] Qiu B, Zhu Q, Du M, et al. Efficient solar light harvesting CdS/Co_9S_8 hollow cubes for z-scheme photocatalytic water splitting. Angew Chem Int Ed 2017;56:2684–8.
[6] Xing M, Zhang J, Qiu B, et al. A brown mesoporous TiO_{2-x}/MCF composite with an extremely high quantum yield of solar energy photocatalysis for H_2 evolution. Small 2015;11:1920–9.
[7] Qiu B, Zhu Q, Xing M, et al. A robust and efficient catalyst of $Cd_xZn_{1-x}Se$ motivated by CoP for photocatalytic hydrogen evolution under sunlight irradiation. Chem Commun 2017;53:897–900.
[8] Xing M, Qiu B, Du M, et al. Spatially separated CdS shells exposed with reduction surfaces for enhancing photocatalytic hydrogen evolution. Adv Funct Mater 2017;27:1702624.
[9] Chen Y, Li W, Jiang D, et al. Facile synthesis of bimodal macroporous g-C_3N_4/SnO_2 nanohybrids with enhanced photocatalytic activity. Sci Bull 2019;64:44–53.
[10] An Y, Li H, Liu Y, et al. Photoelectrical, photophysical and photocatalytic properties of Al based MOFs: MIL-53(Al) and MIL-53-NH_2(Al). J Solid State Chem 2016;233:194–8.
[11] An Y, Liu Y, Wang Z, et al. Stabilizing the titanium-based metal organic frameworks in water by metal cations with empty or partially-filled d orbitals. J Colloid Interface Sci 2019;533:9–12.
[12] Liu Y, Yang Y, Sun Q, et al. Chemical adsorption enhanced CO_2 capture and photoreduction over a copper porphyrin based metal organic framework. ACS Appl Mater Interfaces 2013;5:7654–8.
[13] An Y, Liu Y, An P, et al. Ni^{II} coordination to an Al-based metal-organic framework made from 2-aminoterephthalate for photocatalytic overall water splitting. Angew Chem Int Ed 2017;56:3036–40.
[14] Silva CG, Corma A, García H. Metal-organic frameworks as semiconductors. J Mater Chem 2010;20:3141–56.
[15] Horiuchi Y, Toyao T, Saito M, et al. Visible-light-promoted photocatalytic hydrogen production by using an amino-functionalized Ti(IV) metal-organic framework. J Phys Chem C 2012;116:20848–53.
[16] He X, Gang M, Li Z, et al. Highly conductive and robust composite anion exchange membranes by incorporating quaternized MIL-101(Cr). Sci Bull 2017;62:266–76.
[17] Yan Z-H, Li D, Yin X-B. Review for chiral-at-metal complexes and metal-organic framework enantiomorphs. Sci Bull 2017;62:1344–54.
[18] Liu X, Tang B, Long J, et al. The development of MOFs-based nanomaterials in heterogeneous organocatalysis. Sci Bull 2018;63:502–24.
[19] Meyer K, Ranocchiari M, Bokhoven JA. Metal organic frameworks for photocatalytic water splitting. Energy Environ Sci 2015;8:1923–37.
[20] Wang J-L, Wang C, Lin W. Metal–organic frameworks for light harvesting and photocatalysis. ACS Catal 2012;2:2630–40.
[21] Wang G, Sun Q, Liu Y, et al. A bismuth-based metal–organic framework as an efficient visible-light-driven photocatalyst. Chem Eur J 2015;21:2364–7.
[22] Goh TW, Xiao C, Maligal-Ganesh RV, et al. Utilizing mixed-linker zirconium based metal–organic frameworks to enhance the visible light photocatalytic oxidation of alcohol. Chem Eng Sci 2015;124:45–51.
[23] Chambers MB, Wang X, Ellezam L, et al. Maximizing the photocatalytic activity of metal-organic frameworks with aminated-functionalized linkers: substoichiometric effects in MIL-125-NH_2. J Am Chem Soc 2017;139:8222–8.
[24] Elgrishi N, Chambers MB, Wang X, et al. Molecular polypyridine-based metal complexes as catalysts for the reduction of CO_2. Chem Soc Rev 2017;46:761–96.

[25] Deng X, Albero J, Xu L, et al. Construction of a stable Ru-Re Hybrid system based on multifunctional MOF-253 for efficient photocatalytic CO_2 reduction. Inorg Chem 2018;57:8276–86.
[26] Chambers MB, Wang X, Elgrishi N, et al. Photocatalytic carbon dioxide reduction with rhodium-based catalysts in solution and heterogenized within metal–organic frameworks. ChemSusChem 2015;8:603–8.
[27] Øien S, Agostini G, Svelle S, et al. Probing reactive platinum sites in UiO-67 zirconium metal–organic frameworks. Chem Mater 2015;27:1042–56.
[28] Li X, Zeeland RV, Maligal-Ganesh RV, et al. Impact of linker engineering on the catalytic activity of metal–organic frameworks containing Pd(II)-bipyridine complexes. ACS Catal 2016;6:6324–8.
[29] Choi KM, Kim D, Rungtaweevoranit B, et al. Plasmon-enhanced photocatalytic CO_2 conversion within metal–organic frameworks under visible light. J Am Chem Soc 2017;139:356–62.
[30] Wang C, Xie Z, deKrafft KE, et al. Doping metal–organic frameworks for water oxidation, carbon dioxide reduction, and organic photocatalysis. J Am Chem Soc 2011;133:13445–54.
[31] Braglia L, Borfecchia E, Maddalenaa L, et al. Exploring structure and reactivity of Cu sites in functionalized UiO-67 MOFs. Catal Today 2017;283:89–103.
[32] Yang S, Pattengale B, Lee S, et al. Real-time visualization of active species in a single-site metal–organic framework photocatalyst. ACS Energy Lett 2018;3:532–9.
[33] Fei H, Sampson MD, Lee Y, et al. Photocatalytic CO_2 reduction to formate using a Mn(I) molecular catalyst in a robust metal–organic framework. Inorg Chem 2015;54:6821–8.
[34] Kent CA, Mehl BP, Ma L, et al. Energy transfer dynamics in metal–organic frameworks. J Am Chem Soc 2010;132:12767–9.
[35] Park KC, Seo C, Gupta G, et al. Efficient energy transfer (EnT) in pyrene- and porphyrin-based mixed-ligand metal–organic frameworks. ACS Appl Mater Interfaces 2017;9:38670–7.
[36] Park J, Feng D, Yuan S, et al. Photochromic metal–organic frameworks: reversible control of singlet oxygen generation. Angew Chem Int Ed 2015;54:430–5.
[37] Wu X-P, Gagliardi L, Truhlar DG. Cerium metal–organic framework for photocatalysis. J Am Chem Soc 2018;140:7904–12.
[38] Hendrickx K, Joos JJ, Vos AD, et al. Exploring lanthanide doping in UiO-66: a combined experimental and computational study of the electronic structure. Inorg Chem 2018;57:5463–74.
[39] Wen M, Kuwahara Y, Mori K, et al. Synthesis of Ce ions doped metal–organic framework for promoting catalytic H_2 production from ammonia borane under visible light irradiation. J Mater Chem A 2015;3:14134–41.
[40] Zhang X, Shen B, Zhang X, et al. A comparative study of manganese-cerium doped metal–organic frameworks prepared via impregnation and in situ methods in the selective catalytic reduction of NO. RSC Adv 2017;7:5928–36.
[41] He C-H, Yang O-B. Hydrogen evolution by photocatalytic decomposition of water under UV Irradiation over $K[Bi_3PbTi_5O_{16}]$ perovskite: effect of cerium species. Ind Eng Chem Res 2003;42:419–25.
[42] Rad TS, Khataee A, Pouran SR. Synergistic enhancement in photocatalytic performance of Ce(IV) and Cr(III) co-substituted magnetite nanoparticles loaded on reduced graphene oxide sheets. J Colloid Interface Sci 2018;528:248–62.
[43] Cavka JH, Jakobsen S, Olsbye U, et al. A new zirconium inorganic building brick forming metal organic frameworks with exceptional stability. J Am Chem Soc 2008;130:13850–1.
[44] Jeremias F, Lozan V, Henninger S, et al. Programming MOFs for water sorption: amino-functionalized MIL-125 and UiO-66 for heat transformation and heat storage applications. Dalton Trans 2013;42:15967–73.
[45] Jiang B, Li L, Bian Z, et al. Hydrogen generation from chemical looping reforming of glycerol by Ce doped nickel phyllosilicate nanotube oxygen carriers. Fuel 2018;222:185–92.
[46] Maslakov KI, Teterin YA, Popel AJ, et al. XPS study of ion irradiated and unirradiated CeO_2 bulk and thin film samples. Appl Surface Sci 2018;448:154–62.
[47] Chen X, Chen X, Yu E, et al. In situ pyrolysis of Ce-MOF to prepare CeO_2 catalyst with obviously improved catalytic performance for toluene combustion. Chem Eng J 2018;344:469–79.
[48] Oakes L, Carter R, Hanken T, et al. Interface strain in vertically stacked two-dimensional heterostructured carbon-MoS_2 nanosheets controls electrochemical reactivity. Nat Commun 2016;7:11796.
[49] Liu Y, Zhang N, Yu C, et al. $MnFe_2O_4$@C nanofibers as high-performance anode for sodium-ion batteries. Nano Lett 2016;16:3321–8.
[50] Zhao G, Wang Y, Li X, et al. Quenching electrochemiluminescence immunosensor based on resonance energy transfer between ruthenium (II) complex incorporated in the UiO-67 metal–organic framework and gold nanoparticles for insulin detection. ACS Appl Mater Interfaces 2018;10:22932–8.
[51] Wang J, Zhang J, Peh SB, et al. Dimensional impact of metal-organic frameworks in catalyzing photoinduced hydrogen evolution and cyanosilylation reactions. ACS Appl Energy Mater 2019;2:298–304.
[52] Wu Y, Li B, Wang X, et al. Determination of practical application potential of highly stable UiO-66-AO in Eu(III) elimination investigated by macroscopic and spectroscopic techniques. Chem Eng J 2019;365:249–58.
[53] Wang Y, Yu Y, Li R, et al. Hydrogen production with ultrahigh efficiency under visible light by graphene well-wrapped UiO-66-NH_2 octahedrons. J Mater Chem A 2017;5:20136–40.
[54] Sun D, Liu W, Qiu M, et al. Introduction of a mediator for enhancing photocatalytic performance via post-synthetic metal exchange in metal–organic frameworks (MOFs). Chem Commun 2015;51:2056–9.
[55] Son H-J, Jin S, Patwardhan S, et al. Light-harvesting and ultrafast energy migration in porphyrin-based metal–organic frameworks. J Am Chem Soc 2013;135:862–9.
[56] Guo H, Zhu L, Dang C, et al. Synthesis and photophysical properties of ruthenium(II) polyimine complexes decorated with flavin. Phys Chem Chem Phys 2018;20:17504–16.
[57] Lammert M, Glißmann C, Reinsch H, et al. Synthesis and characterization of new Ce(IV)-MOFs exhibiting various framework topologies. Cryst Growth Des 2017;17:1125–31.
[58] Sapsford KE, Berti L, Medintz IL. Materials for fluorescence resonance energy transfer analysis: beyond traditional donor-acceptor combinations. Angew Chem Int Ed 2006;45:4562–89.
[59] Zhang Q, Zhang C, Cao L, et al. Förster energy transport in metal–organic frameworks is beyond step-by-step hopping. J Am Chem Soc 2016;138:5308–15.
[60] Seres E, Seres J, Serrat C, et al. Core-level attosecond transient absorption spectroscopy of laser-dressed solid films of Si and Zr. Phys Rev B 2016;94:165125.
[61] Portillo AS, Baldoví HG, Fernandez MTG, et al. Ti as mediator in the photoinduced electron transfer of mixed-metal NH_2-UiO-66(Zr/Ti): transient absorption spectroscopy study and application in photovoltaic cell. J Phys Chem C 2017;121:7015–24.
[62] Yan Z-H, Du M-H, Liu J, et al. Photo-generated dinuclear $\{Eu(II)\}_2$ active sites for selective CO_2 reduction in a photosensitizing metal–organic framework. Nat Commun 2018;9:3353.
[63] Yang S, Fan D, Hu W, et al. Elucidating charge separation dynamics in a hybrid metal–organic framework photocatalyst for light-driven H_2 evolution. J Phys Chem C 2018;122:3305–11.

Yang An is working in Institute for Innovative Materials and Energy, Yangzhou University, China. She received her B.S. (2014) degree from Shandong University, and Ph.D. (2019) degree in State Key Laboratory of Crystal Materials, Shandong University. Her research mainly focuses on the design, preparation and photocatalytic activities of MOFs, as well as other nanomaterials.

Yuanyuan Liu is a Professor in State Key Laboratory of Crystal Materials, Shandong University, China. She received her B.S. (2003) degree from Shandong Normal University, and Ph.D. (2008) degree from Institute of Chemistry, Chinese Academy of Sciences. Her research mainly engages in photocatalytic activities of bismuth-based materials, including sulfhydryl-based inorganic semiconductors and bismuth-based organic-inorganic composites.

Baibiao Huang is a Professor in State Key Laboratory of Crystal Materials, Shandong University, China. He received his B.S. (1983), M.S. (1986), Ph.D. (2002) degrees from Shandong University. His research interests focus on (1) compound semiconductor materials and devices; (2) photocatalysis and photochemistry; (3) energy and environmental materials.